ADVANCED ENERGY MATERIALS
www.advenergymat.de

Rethinking the Design of Ionic Conductors Using Meyer–Neldel–Conductivity Plot

Yirong Gao, Nana Li, Yifan Wu, Wenge Yang, and Shou-Hang Bo**

From the discovery of the first fast ionic conductor silver iodide in the early 20th century to the recent discovery of lithium fast ionic conductors with ionic conductivities surpassing those of liquid electrolytes, high ionic conductivity σ has often been associated with low activation energy E_a following the Arrhenius equation. However, the Meyer–Neldel rule (MNR) indicates that the E_a and prefactor σ_0 are correlated, suggesting the relation between the E_a and σ is, in fact, complex. In this perspective, the use of the Meyer–Neldel–conductivity plot and a critical descriptor, Meyer–Neldel energy Δ_0, to guide the search for fast ionic conductors is proposed. Reported lithium, sodium, and magnesium ionic conductors are categorized into three types, depending on the relative magnitude between the Δ_0 and thermal energy (k_BT) at the application temperature. The process by which σ can be optimized by tuning E_a for these types of ionic conductors is elaborated. This principle can be widely applied to all ionic conductors that obey the MNR at any application temperature. Furthermore, a pressure-tuning approach to measure the Δ_0 rapidly is developed. These findings establish a previously missing step for designing new ionic conductors with improved ionic conductivity.

1. Introduction

Fast ionic conductors have been widely used in solid-state batteries, fuel cells, and sensors.[1,2] The replacement of the organic liquid electrolyte with a solid-state electrolyte in emerging solid-state batteries can, in principle, improve battery safety, cycling lifetime, and energy density.[3,4] High-performance applications of solid-state batteries require high ionic conductivity at room temperature, which largely determines their overpotential, and thus, round-trip energy efficiency.[5] Previous studies have identified various lithium, sodium, and even divalent magnesium fast ionic conductors with high room-temperature conductivity at the level of 1 mS cm^{-1}.[6–8] Recently, the sulfide fast ionic conductor $Li_{9.54}Si_{1.74}P_{1.44}S_{11.7}Cl_{0.3}$ reached the room-temperature ionic conductivity of 25 mS cm^{-1}, which even exceeds that of liquid electrolytes.[1] However, these ionic conductors were mostly discovered through chemical intuition and trial and error. Therefore, to guide the selection and identification of the most promising candidates and accelerate the design process, it is urgent to rationalize a general design principle.

In parallel with experimental efforts, computation has greatly advanced our understanding of the relation between structural and physical factors and ion transport.[9–12] Low activation energy had generally been thought to lead to high ionic conductivity. The local structure of the migrating ion along the diffusion path has been shown to strongly affect the activation energy of the ionic conduction.[7,13–15] Ion transport is also considered to correlate to the lattice dynamics. Links between low activation energy and low-energy optical phonons,[16] a soft lattice with highly polarizable anions,[17,18] and a low lithium phonon band center[19,20] have all been proposed. In addition, the low activation energy of fast ionic conductors can be rationalized on the basis of correlated ion transport, where hops of different ions are correlated, partially compensating for the high activation energy required for single-ion hopping.[21,22]

The accepted common ground linking low activation energy to high ionic conductivity is the Arrhenius equation:

$$\sigma T = \sigma_0 e^{\left(-\frac{E_a}{k_B T}\right)} \tag{1}$$

where σ is the ionic conductivity at specific temperature T (in Kelvin), σ_0 is the prefactor, which is commonly presumed to be a constant for a specific class of materials, E_a is the activation energy, and k_B is the Boltzmann constant. From this equation, it is apparent that with a fixed σ_0, lower E_a is expected for higher σ at a fixed temperature. However, as Meyer–Neldel rule (MNR) implies, this "common ground" requires revisiting.[17,18,23,24] The MNR was first proposed by Meyer and Neldel[25] in their study of carrier transport in semiconductor oxides. They observed a linear relation between $\ln\sigma_0$ and E_a in the form of

$$\ln\sigma_0 = \alpha E_a + \beta \tag{2}$$

when the oxygen contents of these oxides were systematically varied by controlling the gas atmosphere of heat treatment.

Y. Gao, Y. Wu, Prof. S.-H. Bo
University of Michigan-Shanghai Jiao Tong University Joint Institute
Shanghai Jiao Tong University
Shanghai 200240, China
E-mail: shouhang.bo@sjtu.edu.cn
Dr. N. Li, Prof. W. Yang
Center for High Pressure Science and Technology Advanced Research (HPSTAR)
Shanghai 201203, China
E-mail: yangwg@hpstar.ac.cn
The ORCID identification number(s) for the author(s) of this article can be found under https://doi.org/10.1002/aenm.202100325.

DOI: 10.1002/aenm.202100325

Here, α and β are constants for a given series of compounds (e.g., ZnO_x), where the reciprocal of α is termed as the Meyer–Neldel energy Δ_0. In fact, this MNR behavior has also been observed in ion transport processes and for a wide range of ionic conductors,[17,23,24,26–35] including Li^+, Na^+, O^{2-}, F^-, H^+, and Ag^+ conductors. Equation (2) shows that the prefactor σ_0 is not a constant, as is often assumed, but rather scales with the activation energy E_a. By combining Equation (1) and (2), the following equation can be obtained:

$$\sigma = \frac{\sigma_0 e^{\left(-\frac{E_a}{k_B T}\right)}}{T} = \frac{e^{\left[\left(\alpha - \frac{1}{k_B T}\right)E_a + \beta\right]}}{T} = \frac{e^{\left[\left(\frac{1}{\Delta_0} - \frac{1}{k_B T}\right)E_a + \beta\right]}}{T} \quad (3)$$

It is clear that the relation between the ionic conductivity σ and activation energy E_a depends on the sign of $\left(\frac{1}{\Delta_0} - \frac{1}{k_B T}\right)$ at a given temperature. This results in the uncertainty of the conductivity variation when the activation energy is changed. Thus, when designing a fast ionic conductor targeting high ionic conductivity through chemical substitutions (or compositional tuning) at a given temperature, the selection of high or low activation energy will depend on the relative magnitude between Δ_0 and the thermal energy $k_B T$.

Herein, we show that the optimization of the ionic conductivity at a specific temperature can still be performed by optimizing the activation energy alone. In contrast to conventional wisdom, however, increased activation energy also can benefit high ionic conductivity when the thermal energy $k_B T$ is higher than Δ_0. To facilitate the optimization of ionic conductivity, we designed the so-called Meyer–Neldel–conductivity (MNC) plot by simultaneously plotting the target ionic conductivity at a specified temperature, activation energy, and prefactor altogether. Using the MNC plot, it becomes clear how the activation energy should be tuned to achieve target ionic conductivity at a given application temperature. We applied this principle to Li-, Na-, and Mg- ionic conductors and categorized them into three different types. In addition, we suggest a pressure-tuning method to rapidly determine the intrinsic Δ_0 with only a single set of measurements for the targeted sample. This approach differs from the typical chemical method, which requires synthesizing and measuring a series of materials with varied compositions.[17,23,24]

2. Results

2.1. MNC Plot and Refined Design Principle of Ionic Conductors

Here, we explain the derivation of the MNC plot and its use to design ionic conductors with improved room-temperature ionic conductivity (**Figure 1**). Taking the logarithm of both sides of Equation (1), the Arrhenius equation can be rearranged as:

$$\ln \sigma_0 = \ln \sigma T + \frac{E_a}{k_B T} \quad (4)$$

For a given ionic conductivity σ (e.g., 1 mS cm^{-1}) at a specific temperature T (e.g., 300 K), $\ln\sigma_0$ is linearly related to the activation energy E_a. Therefore, plotting $\ln\sigma_0$ versus E_a results in straight lines with slopes of $1/k_B T$ and intercepts of $\ln(\sigma T)$ at the y-axis. In Figure 1a, we plot the thermal energy guidelines at a temperature of 300 K (slope^{-1} = 26 meV), and σ values ranging from 10^{-8} to 10^2 mS cm^{-1} are labeled. For a series of materials that follow the MNR (Equation (2)), a straight line is expected in the Meyer–Neldel plot ($\ln\sigma_0$ versus E_a) but with a slope of Δ_0^{-1}. By plotting the Meyer–Neldel plots on top of Figure 1a, we obtain the MNC plots, for example, Figure 1b–d for $Li_6MLa_2Ta_2O_{12}$, $Li_{6+x}P_{1-x}Si_xS_5Br$, and $Li_6PS_5Cl_{1-x}Br_x$, respectively. Because ionic conductors are often used at room temperature, the MNC plots were plotted at 300 K.

Examination of the MNC plots in Figure 1b–d reveals three types of behavior depending on the relative magnitudes of Δ_0 and $k_B T$ (i.e., 26 meV at 300 K). Figure 1b shows the prefactors and activation energies for $Li_6MLa_2Ta_2O_{12}$ compounds (M = Ca, Sr, Ba) with experimental results from Weppner and coworkers.[36] By substituting La^{3+} (24c) with Ca^{2+}, Sr^{2+}, or Ba^{2+} cations, the activation energies of these compounds were systematically varied, and the Δ_0 for the $Li_6MLa_2Ta_2O_{12}$ series was determined to be 115.2 meV, which is much larger than the thermal energy of 26 meV. Consistent with the "common" understanding previously, every 150 meV decrease in activation energy will increase the room-temperature ionic conductivity by two orders of magnitude, as displayed in Figure 1b. The increase in ionic conductivity with decreasing activation energy can also be demonstrated in the plot of conductivity versus activation energy, as shown in Figure 1e.

The activation energies and prefactors for a series of $Li_{6+x}P_{1-x}Si_xS_5Br$ compounds are plotted based on experimental reports from Minafra et al.[37] (Figure 1c). These compounds follow the MNR behavior with a Δ_0 of 19.5 meV, which is much lower than the thermal energy of 26 meV. Interestingly, higher ionic conductivity was, in fact, achieved for the compositions with higher activation energy. This behavior can be clearly observed in Figure 1e.

In the third example, Δ_0 of the argyrodites $Li_6PS_5Cl_{1-x}Br_x$ reported by Kraft[17] was determined to be 23.7 meV, which is close to 26 meV (Figure 1d). The room-temperature ionic conductivity remained in the range of 1.7–3 mS cm^{-1}, regardless of the Cl and Br contents, even though the activation energy changed from 300 to 450 meV (Figure 1d,e).[17] Thus, if a material possesses a Δ_0 close to 26 meV, the ionic conductivity barely changes with the activation energy at 300 K.

The room-temperature experimental data shown in Figure 1 matches very well with the prediction from Equation (3). In practical applications, for example, in solid oxide fuel cells,[38] the working temperature can be very different from room temperature (i.e., 573–1273 K), which will be further discussed later. The corresponding thermal energy $k_B T$ should be selected, serving as the indicator to optimize the ionic conductivity. As a general rule of thumb, at a finite temperature T, if Δ_0 stays above $k_B T$, that is, $\Delta_0 > k_B T$, lower E_a will lead to the higher σ, and we label this type of material as type 1. If $\Delta_0 < k_B T$, higher E_a will lead to higher σ, we label this type of material as type 2. Finally, if $\Delta_0 \approx k_B T$, σ is not sensitive to the change of E_a, and the material is considered type 3. As the correlation between σ and E_a is temperature dependent, the ionic conductor may change to a different type at different working temperatures. For room-temperature applications (i.e., $k_B T$ = 26 meV), we present the conductivity changes with the activation energy for a large number of type 1, 2, and 3 conductors in **Figure 2**a–c, respectively.

We now compare the Δ_0 values of the most common Li-, Na-, and Mg-ionic conductors. The Δ_0 values of these conductors are

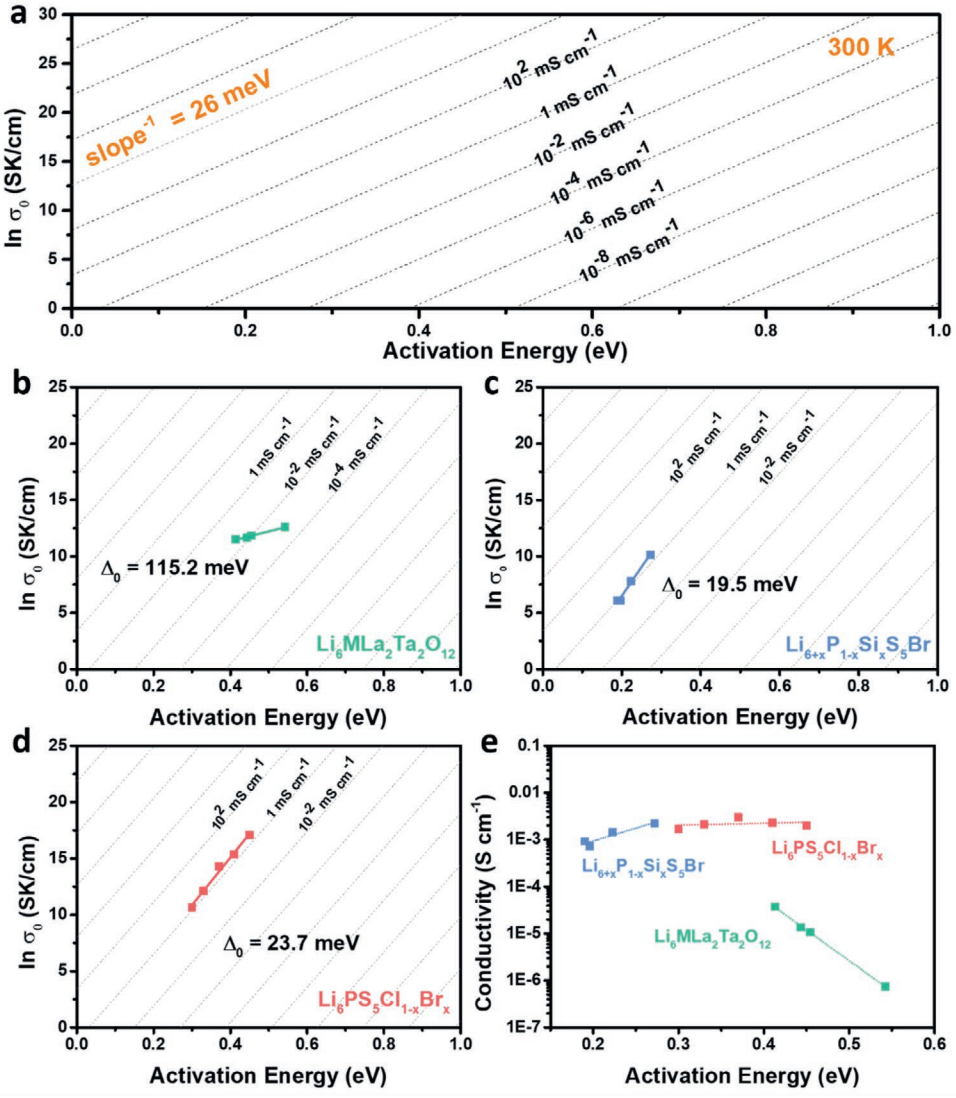

Figure 1. a) Prefactor versus activation energy plot. The dashed lines were obtained using Equation (4), corresponding to different ionic conductivities. These lines share the same slope, and the reciprocal of the slope equals the thermal energy at 300 K, that is, 26 meV. b–d) MNC plots of three types of materials with $\Delta_0 > 26$ meV for $Li_6MLa_2TaO_{12}$ (b),[36] $\Delta_0 < 26$ meV for $Li_{6+x}P_{1-x}Si_xS_5Br$ (c),[37] and $\Delta_0 \approx 26$ meV for $Li_6PS_5Cl_{1-x}Br_x$ (d).[17] e) Conductivity versus activation energy plot of the selected materials in (b–d). The conductivities and prefactors were obtained from refs. [17,36,37].

shown in **Figure 3**, and the Meyer–Neldel plots of these conductors are presented in Figure S1, Supporting Information. All the relevant data obtained from the literature are tabulated in Tables S1–S7, Supporting Information. A broad range of Δ_0 from 15 to 80 meV is observed in Figure 3, which suggests that the materials would correspond to different types of ionic conductors at room temperature according to the classification discussed above. Δ_0 varies with the structure and chemical composition of the material. For example, for thio-LISICON $Li_{10}GeP_2S_{12}$, the partial replacement of the Ge site (4*d*) with isovalent Si or Sn[6,39,40] changes Δ_0 to 33.5 meV, whereas Ge^{4+} cation substitution at the P^{5+} site reduces Δ_0 to 24.9 meV,[41] which provides an interesting example of the transformation of the LISICON system from a type 1 to a type 3 ionic conductor. In garnet $Li_7La_3Zr_2O_{12}$, two aliovalent substitution strategies are commonly used to optimize the ionic conductivity: substitution of La^{3+} (24*c*) with divalent cations, such as Ca^{2+}, Sr^{2+}, or Ba^{2+};[36,65] and substitution of Zr^{4+} (16*a*) with Y^{3+},[42,66] Ta^{5+},[43] or Nb^{5+}.[44] These substitution strategies allow one to tune Δ_0 over an extensive range of 24.6–115.2 meV. At room temperature, substituting Zr^{4+} with Ta^{5+} could bring Δ_0 to ≈26 meV (type 3),[43] which makes the ionic conductivity almost constant over a broad range of activation energies, whereas the other substitutions ($\Delta_0 > 26$ meV) result in significantly increased ionic conductivity with decreased activation energy (type 1).

The type of diffusing ions (e.g., Li^+ versus Na^+ versus Mg^{2+}) also plays an important role in determining the Meyer–Neldel energy. For a similar chemical substitution strategy (i.e., aliovalent substitution at the Zr^{4+} (12*c*) site, producing additional Li, Na, or Mg interstitials), NASICON-structured Li-, Na-, and Mg-ion conductors show drastic differences in Δ_0 (37.7–54.1, 196.4, and 70.9 meV, respectively),

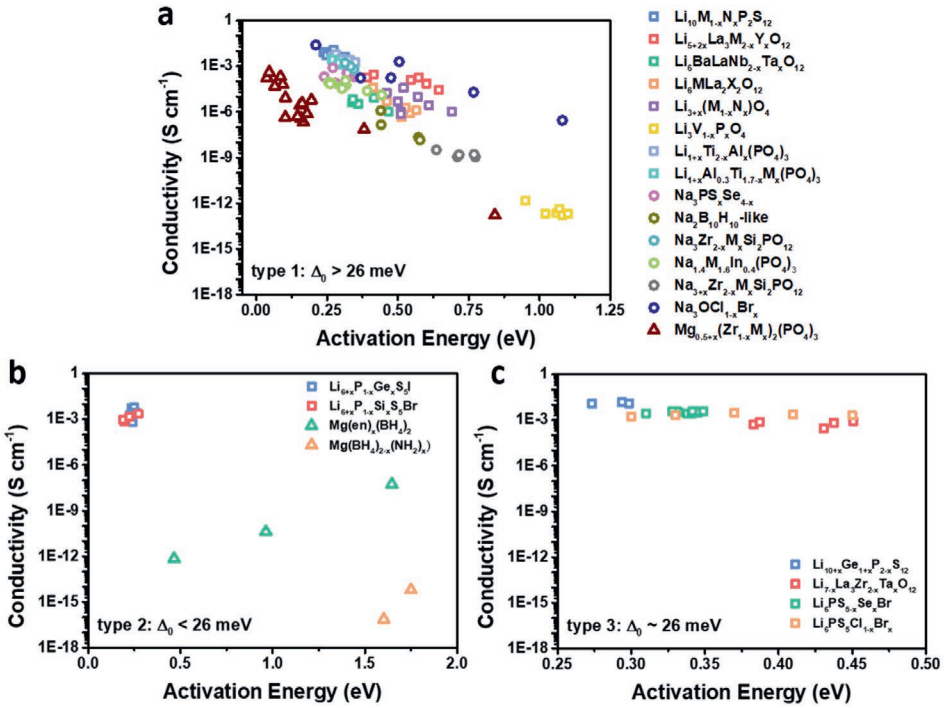

Figure 2. Conductivity versus activation energy of Li-, Na-, and Mg-ionic conductors. These ionic conductors are classified based on the relative magnitude of Δ_0 and the thermal energy at 300 K (26 meV). a), b), and c) correspond to type 1 ($\Delta_0 > 26$ meV), type 2 ($\Delta_0 < 26$ meV), and type 3 ($\Delta_0 \approx 26$ meV) ionic conductors, respectively. Li-, Na-, and Mg-ionic conductors are marked with squares, circles, and triangles, respectively. (All the relevant data are obtained from refs. [1,6,17,23,24,33,36,37,39–64] and detailed information can be found in Tables S1–S7, Supporting Information).

as shown in Figure 3. This finding indicates that Δ_0 strongly depends on the diffusing ions. However, we note that the available data on Na and Mg ionic conductors is relatively scarce compared with that on Li ionic conductors; a comprehensive comparison would require more data on Na and Mg ionic conductors.[67]

2.2. Determination of Meyer–Neldel Energy with Pressure-Tuning Approach

The synthesis of materials with systematically varied compositions is time-consuming and sometimes thermodynamically impossible. The change in activation energy and prefactor with

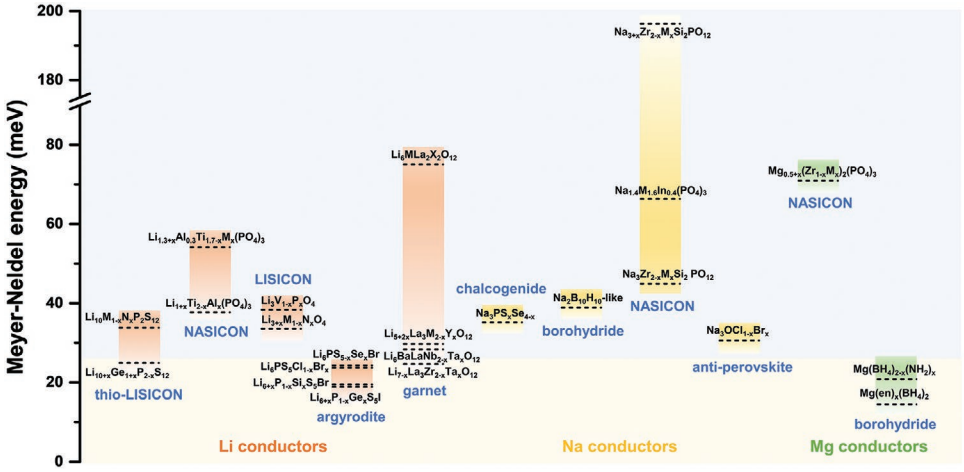

Figure 3. Meyer–Neldel energies Δ_0 of solid-state Li-, Na-, and Mg-ionic conductors. For Li-ionic conductors, various structures are included, such as thio-LISICON, NASICON, LISICON, argyrodite, and garnet. For Na-ionic conductors, the chalcogenide, borohydride, NASICON, and anti-perovskite structure are included. For Mg-ionic conductors, the borohydride and NASICON structure are included. The light-blue and light-yellow backgrounds represent regions with the Δ_0 above and below 26 meV, respectively. Therefore, ionic conductors in the light-blue and light-yellow regions are type 1 and 2 conductors, respectively. The conductors lying near the border are categorized as type 3 conductors. For the ionic conductivity behavior at different temperatures, the borderline can be adjusted based on the value of k_BT. (All the relevant data obtained from previous literature can be found in Tables S1–S7, Supporting Information).

chemical composition variation can also be small, making reliable extrapolation of Meyer–Neldel energy difficult. In addition, doping and chemical substitution may introduce local disorder and inhomogeneity, which can also affect the ion-transport property to a large extent.[68] Here, we propose an alternative pressure-tuning method to rapidly determine Δ_0. We select the cubic garnet lithium ionic conductor $Li_{6.4}La_3Zr_{1.4}Ta_{0.6}O_{12}$ (LLZTO) as an example to explain our approach below. LLZTO is one of the most promising candidates for solid-state lithium batteries, with high ionic conductivity, air stability, and apparent electrochemical stability against lithium metal.[69] Detailed characterization results of pristine LLZTO obtained through inductively coupled plasma spectroscopy, X-ray diffraction (XRD), and Raman spectroscopy are presented in Table S8 and Figures S2a, and S2b, Supporting Information, respectively.

We utilized the diamond anvil cell (DAC) technique to modify the sample pressure environment. LLZTO powder was pressed into a micro pellet and loaded into a metal gasket along with a ruby sphere for pressure monitoring.[70] The structural evolution under high pressure was determined by synchrotron XRD data (Beamline 13-BM-C at the Advanced Photon Source, Argonne National Laboratory) up to 23.6 GPa followed by decompression to ambient condition. The powder diffraction patterns can be well fitted to the ambient cubic phase with space group $Ia\bar{3}d$ (No. 230) up to 11.5 GPa (Figure S3, Supporting Information). With further compression, we observed the onset of a phase transition at a pressure of 14.4 GPa changing to a lower symmetry structure (Figure S4, Supporting Information). The diffraction data from 14.4 to 23.6 GPa can be indexed as a tetragonal phase, the discussion of which is beyond the scope of this work. It is worth noting that upon decompression to ambient pressure, the crystal structure returned to its original cubic garnet phase (Figure S5, Supporting Information), indicating that the pressure-induced phase transition is reversible.

We then focused on the ion-transport properties of LLZTO within the cubic-phase pressure range with variable-temperature impedance measurements. **Figure 4** presents the impedance spectra measured at 25 °C at selected pressures. The typical low-frequency linear response of the Nyquist plot gradually disappeared with increasing pressure, indicating a change from ion-dominant conduction to ion-electron mixed conduction.[71] Below 5.98 GPa, ion conduction dominated, while the electron contribution gradually grew with increasing pressure. To accurately extract both the ionic and electronic conductivity, different equivalent circuits were selected to fit the impedance spectra below and above 5.98 GPa (details are presented in Figure S6, Supporting Information). The electronic conductivities were also measured using the DC polarization method (Figure S7, Supporting Information), showing great consistency with the values fitted from the impedance spectra (Table S9, Supporting Information).

Variable-temperature impedance measurements were performed in the range of 25–65 °C and from 2.55 to 11.37 GPa (Figure S10, Supporting Information). This allowed us to determine the activation energy and prefactor at each pressure (Table S10, Supporting Information) as well as Δ_0. The prefactors of $Li_{6.4}La_3Zr_{1.4}Ta_{0.6}O_{12}$ at different pressures were observed to scale with the activation energies (**Figure 5**), closely following the MNR and Δ_0 was determined to be 26.3 meV. The cubic

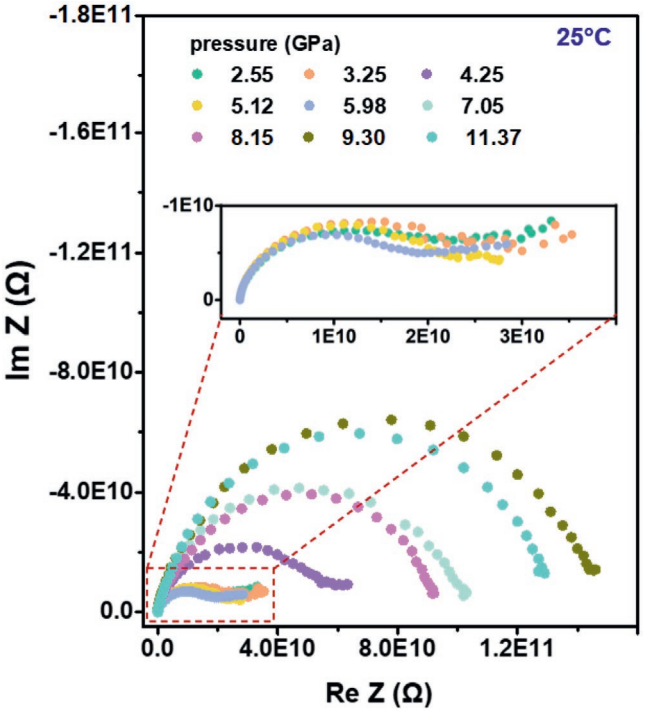

Figure 4. Impedance spectra of $Li_{6.4}La_3Zr_{1.4}Ta_{0.6}O_{12}$ at room temperature and different pressures. The inset presents a zoomed-in view of the dashed rectangle region.

LLZTO studied in this high-pressure work was Ta substituted at the Zr site (16*a*). For comparison, data from a series of chemically-substituted $Li_{7-x}La_3Zr_{2-x}Ta_xO_{12}$ compounds reported by Hamao et al.[43] were plotted, and the Δ_0 was determined to be 24.6 meV, close to the value obtained in the current study using a high pressure-tuning method (Figure 5). We further note that Δ_0 of garnets with different chemical substitution strategies differed (Figure S11, Supporting Information). The activation

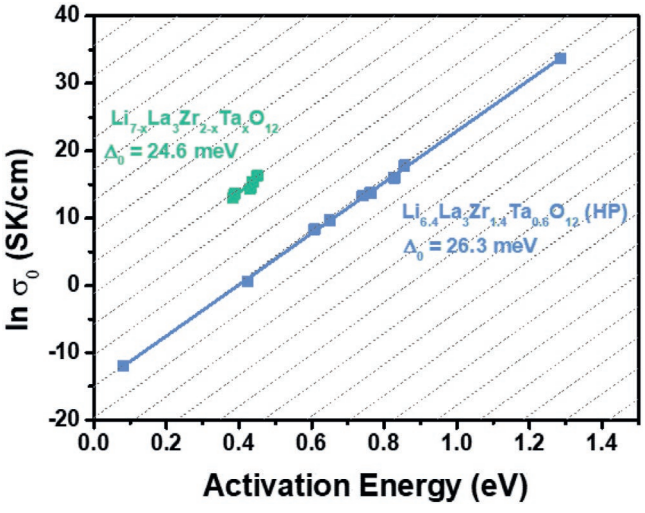

Figure 5. MNC plots at 300 K for $Li_{6.4}La_3Zr_{1.4}Ta_{0.6}O_{12}$ under pressures from 2.55 to 11.37 GPa (this work, shown in blue) and chemically substituted $Li_{7-x}La_3Zr_{2-x}Ta_xO_{12}$ (data is obtained from ref. [43], shown in green).

energy changes achieved by chemical substitutions were limited to approximately 0.2 eV, whereas the high-pressure tuning resulted in a 1.2 eV change (0.1 to 1.3 eV) with an excellent linear MNR relation, making the determination of Δ_0 much more precise. As Δ_0 is close to 26 meV, although the activation energy underwent an order of magnitude change from 0.1 to 1.3 eV, the room-temperature ionic conductivity for LLZTO remained almost constant (Figure S11b, Supporting Information).

3. Discussion

3.1. Wide Applicability of Meyer–Neldel–Conductivity Plot for Carrier Transport

The ionic and electronic conductivities of cubic garnets vary substantially with pressure. From ambient pressure to 2.55 GPa, the room temperature ionic conductivity of LLZTO sharply drops from 3.29×10^{-4} to 9.1×10^{-10} S cm^{-1} and electronic conductivity from 7.96×10^{-8} to 5.9×10^{-10} S cm^{-1} (Figure S9a, Supporting Information), leading to four orders of magnitude decrease of the ratio of the ionic and electronic conductivities (Figure S9b, Supporting Information). The results indicate that the intrinsic conductivity of both ion and electron of solid-state electrolytes and their ratio can be simultaneously changed with pressure, which may alter the location of lithium deposition (e.g., close to the current collector or inside the solid-state electrolyte), potentially leading to short circuits.[72] Inspired by recent works which explored the pressure effect on the stripping and plating of lithium metal in solid-state batteries,[73,74] we believe that it is equally important to explore intrinsic ionic and electronic conductivities of solid-state electrolytes. Intriguingly, we further studied the electronic conductivity of LLZTO from 2.55 to 11.37 GPa and found that it also followed the MNR with a Meyer–Neldel energy of 27.52 meV, as shown in **Figure 6**a. This suggests that our method (i.e., the MNC plot, pressure-tuning method, and refined design principle) can also be applied to tune electronic conductivity. Following the guideline proposed above, the electronic conductivity of our LLZTO sample barely changes against activation energy from 2.55 to 11.37 GPa. Thus, it is a type 3 conductor in terms of electronic transport and its relation between conductivity and activation energy is shown in Figure 6b.

Besides using our refined design principle at room temperature, it can also be used at high temperatures that are of interest for solid oxide fuel cells (e.g., 573 to 1273 K). Here, we took the oxide conductors as an example. The Meyer–Neldel–conductivity plot and the corresponding Meyer–Neldel energy are shown in **Figure 7** and Table S11, Supporting Information. The selected oxide conductors $(Ce_{0.8}Sm_{0.2})_{1-x}Sr_xO_{2-\delta}$[75] (blue squares in Figure 7a) and $(Ce_{0.38}Sm_{0.17})_{1-x}Zr_xO_{2-\delta}$[76] (red squares in Figure 7a) are crystallized in the fluorite structure (space group $Fm\bar{3}m$, No. 225), where Ce, Sm, and Sr or Zr are statistically distributed in the Wyckoff position *4a*. The Meyer–Neldel energy of these are 211.5 and 395.8 meV, respectively. Another case is the apatite structure oxide conductors $La_{10}Si_6O_{27}$, shown in Figure 7b. The materials with substitutions at the La-site $La_9MSi_6O_{26.5}$[77] and at the Si-site $La_{10}Si_{5.5}M_{0.5}O_{27+\delta}$[78] have the Meyer–Neldel energies of 32.0 and 55.8 meV, respectively. As most solid oxide fuel cells operate at 573 to 1273 K, we choose the MNC plot at 773 K (500 °C) where the thermal energy k_BT is 67 meV, as shown in Figure 7. According to the principle we propose in this work, if the conductors are used at 773 K, lower activation energy is beneficial to obtaining higher ionic conductivity for the fluorite structure system (i.e., type 1 conductors). In comparison, higher activation energy will lead to higher conductivity for apatite structured materials (i.e., type 2 conductors). The trends of ionic conductivity change at 773 K with respect to the activation energy are shown in Figure 7c,d.

Based on the above discussion in various systems, including the Li-, Na-, and Mg-ionic conductors used at room temperature and the oxide conductors used at high temperature, the common notion that low activation energy is beneficial for high ionic conductivity has been overturned. We have elaborated the correlations between ionic conductivity and activation energy for different ionic conductors, which critically depends on the relative magnitude of Meyer–Neldel energy Δ_0 and the thermal energy k_BT at a given application temperature. Therefore, is there any physical meaning associated with Δ_0? If yes, how does Δ_0 correlate with the intrinsic physical or structural parameters of a material? Answers to these questions are important in refining the design principle of ionic conductors.

4. Conclusion

A general principle with thorough consideration of both prefactor and activation energy in the Arrhenius equation leads to the categorization of three types of ionic conductors depending on the

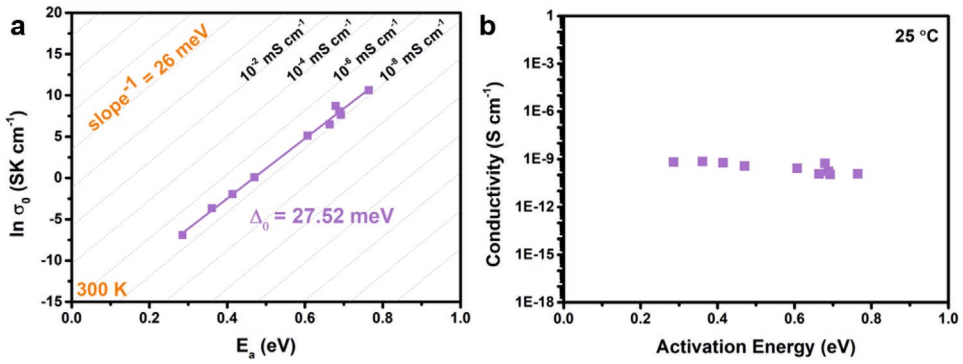

Figure 6. a) MNC plot and b) plot of conductivity versus activation energy of $Li_{6.4}La_3Zr_{1.4}Ta_{0.6}O_{12}$ under high pressure (from 2.55 to 11.37 GPa), where the conductivity here refers to the electronic conductivity as determined from our DC measurement at various pressures.

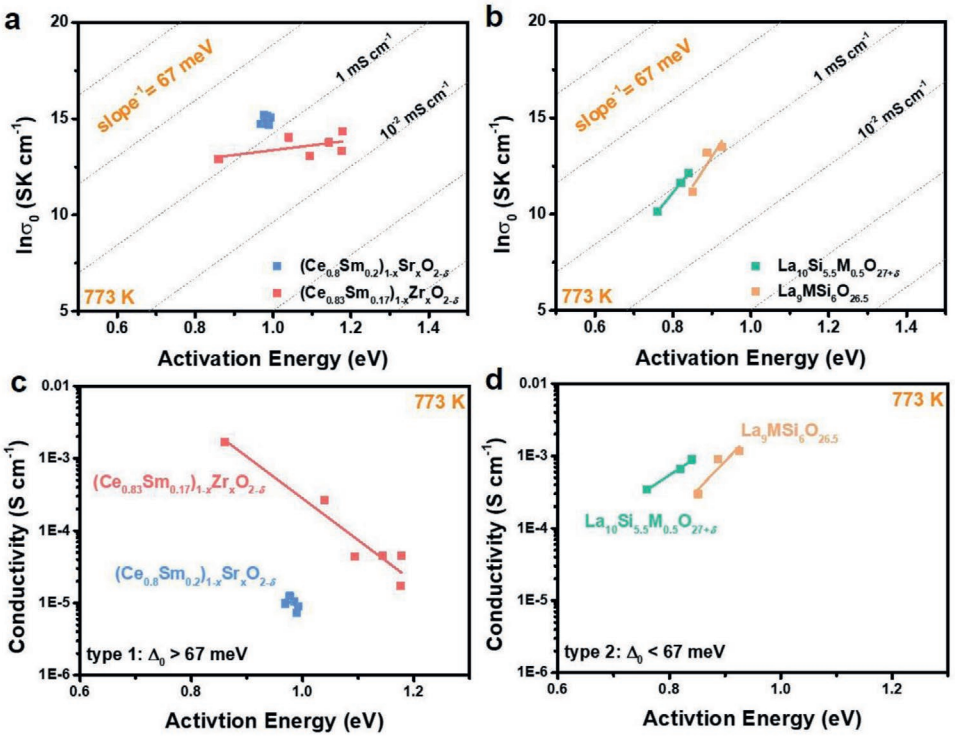

Figure 7. a,b) The MNC plot and c,d) the plot of ionic conductivity versus activation energy at 773 K of oxide conductors, including the cubic fluorite structure $(Ce_{0.8}Sm_{0.2})_{1-x}Sr_xO_{2-\delta}$[75] (blue squares in panel (a,c)) and $(Ce_{0.38}Sm_{0.17})_{1-x}Zr_xO_{2-\delta}$[76] (red squares in panel (a,c)), and the apatite structure $La_{10}Si_{5.5}M_{0.5}O_{27+\delta}$[77] (green squares in panel (b,d)) and $La_9MSi_6O_{26.5}$[78] (orange squares in panel (b,d)). Data are obtained from refs. [75–78]. Tabulated data can be found in Table S11, Supporting Information.

relative magnitude of Meyer–Neldel energy Δ_0 of the materials and the thermal energy k_BT at the application temperature. We showed that the long-held belief of improving the ionic conductivity by decreasing the activation energy is only valid for certain cases (i.e., type 1 conductors). For room-temperature applications, the thermal energy k_BT is 26 meV. For type 1 ionic conductors ($\Delta_0 > 26$ meV), lower activation energy leads to higher ionic conductivity; for type 2 ($\Delta_0 < 26$ meV), higher activation energy leads to higher ionic conductivity; and for type 3 ionic conductors ($\Delta_0 \approx 26$ meV), the ionic conductivity does not change with activation energy. This principle is universal to all ionic conductors that obey the MNR. As long as the Meyer–Neldel energy is known, the optimization of ionic conductivity at a given temperature can still be achieved by tuning the activation energy alone. Therefore, for a given ionic conductor, we should first measure or compute its Meyer–Neldel energy. Then, through compositional tuning or other structural modifications, we can target either to decrease or increase the activation energy depending on the relative magnitude between the Meyer–Neldel energy and thermal energy k_BT. Thus, our work provides new and valuable conductivity-oriented guidelines for the development of solid-state ionic conductors with improved ionic conductivity.

5. Experimental Section

Sample Characterization at Ambient Conditions: Garnet $Li_{6.4}La_3Zr_{1.4}Ta_{0.6}O_{12}$ (LLZTO) was purchased from Kejing, MTI (purity 99.99%). The purity and composition of $Li_{6.4}La_3Zr_{1.4}Ta_{0.6}O_{12}$ were verified using X-ray diffraction (Bruker D8 DaVinci) using Cu Kα radiation, Raman spectroscopy (Bruker Optics Senterra R200-L) using a 532 nm green laser, and inductively coupled plasma spectroscopy (Thermo iCAP7600). All these measurements were performed at the Instrumental Analysis Center of Shanghai Jiao Tong University.

The powder was cold pressed into a pellet without a binder (≈1 mm thick) with uniaxial pressing at a pressure of 5 tons in a stainless-steel die with a diameter of 1.2 cm. The pressed pellet was then calcined at 1130 °C for 12 h in an Al_2O_3 crucible. After calcination, the pellet was sputtered with Pt on both sides for AC impedance and DC polarization measurement. The AC impedance measurement was conducted using a Solartron Materials Testing System in a Swagelok cell with an AC amplitude of 10 mV and frequency ranging from 1 MHz to 0.005 Hz. The DC polarization was measured with an input voltage of 2 V for 600 s. The variable-temperature impedance was measured in the range of −15 to 25°C.

Sample Fabrication and Characterization under High Pressure: DACs with culet diameter of 300 and 500 µm were used for the high-pressure XRD and impedance experiments, respectively. The sample and ruby were loaded into the sample chamber, and the pressure inside the DAC was determined based on the luminescence shift of ruby under high pressure.

The in situ high-pressure XRD measurements of LLZTO at high pressure were conducted at beamline 13-BM-C at the Advanced Photon Source (APS) of Argonne National Laboratory using a monochromatic X-ray beam with wavelength 0.434 Å. The pressure was increased up to 23.6 GPa at room temperature, and neon was used as the pressure medium. The Pawley refinements were performed using the TOPAS 4.2 software package (Bruker).

The impedance spectra were measured with the two-plate Pt electrodes in the DAC. The high-pressure impedance measurement sample was a micro pellet with a diameter of ≈200 µm and thickness of 40 µm. No pressure medium was used to avoid the introduction of

impurities. The high-pressure impedance and DC measurements were conducted using a Solartron Materials Testing System in the pressure range of 2.55–11.37 GPa. For AC measurements, a 100 mV AC amplitude and a frequency range of 1 MHz to 0.005 Hz were used. The electronic conductivities at different temperatures were measured by applying a 2 V DC voltage. For the variable-temperature measurement, a standard K-type thermometer was placed on the side of the DAC to calibrate the temperature. The variable-temperature impedance was measured in the range of 25–65 °C. To ensure that the sample temperature reached the set temperature, the sample was held for 2 h at the target temperature before the AC and DC measurements.

Supporting Information

Supporting Information is available from the Wiley Online Library or from the author.

Acknowledgements

Y.G. and N.L. contributed equally to this work. This work was supported by the National Natural Science Foundation of China (Grant Nos. 51902201, 51527801). Portions of this work were performed at GeoSoilEnviroCARS (The University of Chicago, Sector 13), Advanced Photon Source (APS), Argonne National Laboratory. GeoSoilEnviroCARS is supported by the National Science Foundation–Earth Sciences (EAR–1634415) and Department of Energy-GeoSciences (DE–FG02–94ER14466). This research used resources of the Advanced Photon Source, a U.S. Department of Energy (DOE) Office of Science User Facility operated for the DOE Office of Science by Argonne National Laboratory under Contract No. DE-AC02-06CH11357. The authors also acknowledge Dr. Dongzhou Zhang of 13-BMC at GSECARS, APS for technical support.

Conflict of Interest

The authors declare no conflict of interest.

Keywords

activation energy, high ionic conductivity, Meyer–Neldel rule, solid-state ionic conductors

Received: January 28, 2021
Published online:

[1] Y. Kato, S. Hori, T. Saito, K. Suzuki, M. Hirayama, A. Mitsui, M. Yonemura, H. Iba, R. Kanno, *Nat. Energy* **2016**, *1*, 16030.
[2] M. Struzik, I. Garbayo, R. Pfenninger, J. L. M. Rupp, *Adv. Mater.* **2018**, *30*, 1804098.
[3] J. Li, C. Ma, M. Chi, C. Liang, N. J. Dudney, *Adv. Energy Mater.* **2015**, *5*, 1401408.
[4] Y.-G. Lee, S. Fujiki, C. Jung, N. Suzuki, N. Yashiro, R. Omoda, D.-S. Ko, T. Shiratsuchi, T. Sugimoto, S. Ryu, J. H. Ku, T. Watanabe, Y. Park, Y. Aihara, D. Im, I. T. Han, *Nat. Energy* **2020**, *5*, 299.
[5] T. Famprikis, P. Canepa, J. A. Dawson, M. S. Islam, C. Masquelier, *Nat. Mater.* **2019**, *18*, 1278.
[6] N. Kamaya, K. Homma, Y. Yamakawa, M. Hirayama, R. Kanno, M. Yonemura, T. Kamiyama, Y. Kato, S. Hama, K. Kawamoto, A. Mitsui, *Nat. Mater.* **2011**, *10*, 682.
[7] P. Canepa, S.-H. Bo, G. S. Gautam, B. Key, W. D. Richards, T. Shi, Y. Tian, Y. Wang, J. Li, G. Ceder, *Nat. Commun.* **2017**, *8*, 1759.
[8] J. L. Briant, G. C. Farrington, *J. Solid State Chem.* **1980**, *33*, 385.
[9] S. P. Ong, Y. Mo, W. D. Richards, L. Miara, H. S. Lee, G. Ceder, *Energy Environ. Sci.* **2013**, *6*, 148.
[10] P. Bron, S. Johansson, K. Zick, J. Schmedt auf der Gunne, S. Dehnen, B. Roling, *J. Am. Chem. Soc.* **2013**, *135*, 15694.
[11] W. D. Richards, T. Tsujimura, L. J. Miara, Y. Wang, J. C. Kim, S. P. Ong, I. Uechi, N. Suzuki, G. Ceder, *Nat. Commun.* **2016**, *7*, 11009.
[12] V. S. Kandagal, M. D. Bharadwaj, U. V. Waghmare, *J. Mater. Chem. A* **2015**, *3*, 12992.
[13] Y. Wang, W. D. Richards, S. P. Ong, L. J. Miara, J. C. Kim, Y. Mo, G. Ceder, *Nat. Mater.* **2015**, *14*, 1026.
[14] A. Duvel, P. Heitjans, P. Fedorov, G. Scholz, G. Cibin, A. V. Chadwick, D. M. Pickup, S. Ramos, L. W. L. Sayle, E. K. L. Sayle, T. X. T. Sayle, D. C. Sayle, *J. Am. Chem. Soc.* **2017**, *139*, 5842.
[15] X. He, Q. Bai, Y. Liu, A. M. Nolan, C. Ling, Y. Mo, *Adv. Energy Mater.* **2019**, *9*, 1902078.
[16] K. Wakamura, *Phys. Rev. B* **1997**, *56*, 11593.
[17] M. A. Kraft, S. P. Culver, M. Calderon, F. Böcher, T. Krauskopf, A. Senyshyn, C. Dietrich, A. Zevalkink, J. Janek, W. G. Zeier, *J. Am. Chem. Soc.* **2017**, *139*, 10909.
[18] T. Krauskopf, S. Muy, S. P. Culver, S. Ohno, O. Delaire, Y. Shao-Horn, W. G. Zeier, *J. Am. Chem. Soc.* **2018**, *140*, 14464.
[19] S. Muy, J. C. Bachman, L. Giordano, H.-H. Chang, D. L. Abernathy, D. Bansal, O. Delaire, S. Hori, R. Kanno, F. Maglia, S. Lupart, P. Lamp, Y. Shao-Horn, *Energy Environ. Sci.* **2018**, *11*, 850.
[20] S. Muy, J. Voss, R. Schlem, R. Koerver, S. J. Sedlmaier, F. Maglia, P. Lamp, W. G. Zeier, Y. Shao-Horn, *iScience* **2019**, *16*, 270.
[21] X. He, Y. Zhu, Y. Mo, *Nat. Commun.* **2017**, *8*, 15893.
[22] Z. Zou, N. Ma, A. Wang, Y. Ran, T. Song, Y. Jiao, J. Liu, H. Zhou, W. Shi, B. He, D. Wang, Y. Li, M. Avdeev, S. Shi, *Adv. Energy Mater.* **2020**, *10*, 2001486.
[23] S. Muy, J. C. Bachman, H.-H. Chang, L. Giordano, F. Maglia, S. Lupart, P. Lamp, W. G. Zeier, Y. Shao-Horn, *Chem. Mater.* **2018**, *30*, 5573.
[24] T. Krauskopf, C. Pompe, M. A. Kraft, W. G. Zeier, *Chem. Mater.* **2017**, *29*, 8859.
[25] V. W. Meyer, H. Neldel, *Z. Tech. Phys.* **1937**, *12*, 588.
[26] R. Metselaar, G. Oversluizen, *J. Solid State Chem.* **1984**, *55*, 320.
[27] J. H. Schön, *Defect Diffus. Forum* **2001**, *192–193*, 37.
[28] K. Shimakawa, F. Abdel-Wahab, *Appl. Phys. Lett.* **1997**, *70*, 652.
[29] S. D. Savransky, A. Yelon, *Phys. Status Solidi A* **2010**, *207*, 627.
[30] H. Meiling, R. E. I. Schropp, *Appl. Phys. Lett.* **1999**, *74*, 1012.
[31] H. Overhof, P. Thomas, *Defect Diffus. Forum* **2001**, *192–193*, 1.
[32] D. P. Almond, A. R. West, *Solid State Ionics* **1986**, *18–19*, 1105.
[33] T. Bernges, S. P. Culver, N. Minafra, R. Koerver, W. G. Zeier, *Inorg. Chem.* **2018**, *57*, 13920.
[34] A. S. Nowick, W.-K. Lee, H. Jain, *Solid State Ionics* **1988**, *28–30*, 89.
[35] A. Braun, Q. Chen, A. Yelon, *Chimia* **2019**, *73*, 936.
[36] R. Murugan, V. Thangadurai, W. Weppnera, *J. Electrochem. Soc.* **2008**, *155*, A90.
[37] N. Minafra, S. P. Culver, T. Krauskopf, A. Senyshyn, W. G. Zeier, *J. Mater. Chem. A* **2018**, *6*, 645.
[38] E. Fabbri, D. Pergolesi, E. Traversa, *Chem. Soc. Rev.* **2010**, *39*, 4355.
[39] T. Krauskopf, S. P. Culver, W. G. Zeier, *Chem. Mater.* **2018**, *30*, 1791.
[40] Y. Kato, R. Saito, M. Sakano, A. Mitsui, M. Hirayama, R. Kanno, *J. Power Sources* **2014**, *271*, 60.
[41] O. Kwon, M. Hirayama, K. Suzuki, Y. Kato, T. Saito, M. Yonemura, T. Kamiyama, R. Kanno, *J. Mater. Chem. A* **2015**, *3*, 438.
[42] A. K. Baral, S. Narayanan, F. Ramezanipour, V. Thangadurai, *Phys. Chem. Chem. Phys.* **2014**, *16*, 11356.
[43] N. Hamao, K. Kataoka, N. Kijima, J. Akimoto, *J. Ceram. Soc. Jpn.* **2016**, *124*, 678.

[44] Y. Zhong, Q. Zhou, Y. Guo, Z. Li, Y. Qiang, *Ionics* **2013**, *19*, 697.
[45] K. Arbi, R. Jimenez, T. Šalkus, A. F. Orliukas, J. Sanz, *Solid State Ionics* **2015**, *271*, 28.
[46] M. A. Kraft, S. Ohno, T. Zinkevich, R. Koerver, S. P. Culver, T. Fuchs, A. Senyshyn, S. Indris, B. J. Morgan, W. G. Zeier, *J. Am. Chem. Soc.* **2018**, *140*, 16330.
[47] S. Narayanan, A. K. Baral, V. Thangadurai, *Phys. Chem. Chem. Phys.* **2016**, *18*, 15418.
[48] V. Thangadurai, W. Weppner, *J. Am. Ceram. Soc.* **2005**, *88*, 411.
[49] S.-H. Bo, Y. Wang, G. Ceder, *J. Mater. Chem. A* **2016**, *4*, 9044.
[50] T. J. Udovic, M. Matsuo, W. S. Tang, H. Wu, V. Stavila, A. V. Soloninin, R. V. Skoryunov, O. A. Babanova, A. V. Skripov, J. J. Rush, *Adv. Mater.* **2014**, *26*, 7622.
[51] W. S. Tang, M. Matsuo, H. Wu, V. Stavila, A. Unemoto, S.-i. Orimo, T. J. Udovic, *Energy Storage Mater.* **2016**, *4*, 79.
[52] W. S. Tang, M. Matsuo, H. Wu, V. Stavila, W. Zhou, A. A. Talin, A. V. Soloninin, R. V. Skoryunov, O. A. Babanova, A. V. Skripov, *Adv. Energy Mater.* **2016**, *6*, 1502237.
[53] W. S. Tang, A. Unemoto, W. Zhou, V. Stavila, M. Matsuo, H. Wu, S. I. Orimo, T. J. Udovic, *Energy Environ. Sci.* **2015**, *8*, 3637.
[54] H. Park, K. Jung, M. Nezafati, C. S. Kim, B. Kang, *ACS Appl. Mater. Interfaces* **2016**, *8*, 27814.
[55] D. Chen, F. Luo, W. Zhou, D. Zhu, *J. Alloys Compd.* **2018**, *757*, 348.
[56] E. R. Losilla, M. A. G. Aranda, S. Bruque, M. A. París, J. Sanz, A. R. West, *Chem. Mater.* **1998**, *10*, 665.
[57] S. K. Pal, R. Saha, G. V. Kumar, S. Omar, *J. Phys. Chem. C* **2020**, *124*, 9161.
[58] Y. Wang, Q. Wang, Z. Liu, Z. Zhou, S. Li, J. Zhu, R. Zou, Y. Wang, J. Lin, Y. Zhao, *J. Power Sources* **2015**, *293*, 735.
[59] M. Adamu, G. M. Kale, *J. Phys. Chem. C* **2016**, *120*, 17909.
[60] N. K. Anuar, S. B. R. S. Adnan, N. S. Mohamed, *Ceram. Int.* **2014**, *40*, 13719.
[61] N. K. Anuar, N. S. Mohamed, *J. Sol-Gel Sci. Technol.* **2016**, *80*, 249.
[62] N. K. Anuar, S. B. R. S. Adnan, M. H. Jaafar, N. S. Mohamed, *Ionics* **2016**, *22*, 1125.
[63] S. Higashi, K. Miwa, M. Aoki, K. Takechi, *Chem. Commun.* **2014**, *50*, 1320.
[64] E. Roedern, R. S. Kuhnel, A. Remhof, C. Battaglia, *Sci. Rep.* **2017**, *7*, 46189.
[65] V. Thangadurai, H. Kaack, W. J. F. Weppner, *J. Am. Ceram. Soc.* **2003**, *86*, 437.
[66] S. Narayanan, V. Thangadurai, *J. Power Sources* **2011**, *196*, 8085.
[67] P. W. Jaschin, Y. Gao, Y. Li, S.-H. Bo, *J. Mater. Chem. A* **2020**, *8*, 2875.
[68] Y. Gao, A. M. Nolan, P. Du, Y. Wu, C. Yang, Q. Chen, Y. Mo, S.-H. Bo, *Chem. Rev.* **2020**, *120*, 5954.
[69] C. Wang, K. Fu, S. P. Kammampata, D. W. McOwen, A. J. Samson, L. Zhang, G. T. Hitz, A. M. Nolan, E. D. Wachsman, Y. Mo, V. Thangadurai, L. Hu, *Chem. Rev.* **2020**, *120*, 4257.
[70] H. K. Mao, J. Xu, P. M. Bell, *J. Geophys. Res.* **1986**, *91*, 4673.
[71] R. A. Huggins, *Ionics* **2002**, *8*, 300.
[72] F. Han, A. S. Westover, J. Yue, X. Fan, F. Wang, M. Chi, D. N. Leonard, N. J. Dudney, H. Wang, C. Wang, *Nat. Energy* **2019**, *4*, 187.
[73] J. M. Doux, H. Nguyen, D. H. S. Tan, A. Banerjee, X. Wang, E. A. Wu, C. Jo, H. Yang, Y. S. Meng, *Adv. Energy Mater.* **2019**, *10*, 1903253.
[74] M. J. Wang, R. Choudhury, J. Sakamoto, *Joule* **2019**, *3*, 2165.
[75] Y. Zheng, S. He, L. Ge, M. Zhou, H. Chen, L. Guo, *Int. J. Hydrogen Energy* **2011**, *36*, 5128.
[76] W. Huang, P. Shuk, M. Greenblatt, M. Croft, F. Chen, M. Liu, *J. Electrochem. Soc.* **2000**, *147*, 4196.
[77] J. Xiang, Z.-G. Liu, J.-H. Ouyang, Y. Zhou, F.-Y. Yan, *Solid State Ionics* **2012**, *220*, 7.
[78] L. Zhang, H. Q. He, H. Wu, C.-Z. Li, S. P. Jiang, *Int. J. Hydrogen Energy* **2011**, *36*, 6862.